

# A Feshbach resonance in collisions between triplet ground-state molecules

<https://doi.org/10.1038/s41586-022-05635-8>

Juliana J. Park<sup>1</sup>✉, Yu-Kun Lu<sup>1</sup>, Alan O. Jamison<sup>2,3</sup>, Timur V. Tscherbul<sup>4</sup> & Wolfgang Ketterle<sup>1</sup>

Received: 10 August 2022

Accepted: 6 December 2022

Published online: 1 February 2023

 Check for updates

Collisional resonances are important tools that have been used to modify interactions in ultracold gases, for realizing previously unknown Hamiltonians in quantum simulations<sup>1</sup>, for creating molecules from atomic gases<sup>2</sup> and for controlling chemical reactions. So far, such resonances have been observed for atom–atom collisions, atom–molecule collisions<sup>3–7</sup> and collisions between Feshbach molecules, which are very weakly bound<sup>8–10</sup>. Whether such resonances exist for ultracold ground-state molecules has been debated owing to the possibly high density of states and/or rapid decay of the resonant complex<sup>11–15</sup>. Here we report a very pronounced and narrow (25 mG) Feshbach resonance in collisions between two triplet ground-state NaLi molecules. This molecular Feshbach resonance has two special characteristics. First, the collisional loss rate is enhanced by more than two orders of magnitude above the background loss rate, which is saturated at the *p*-wave universal value, owing to strong chemical reactivity. Second, the resonance is located at a magnetic field where two open channels become nearly degenerate. This implies that the intermediate complex predominantly decays to the second open channel. We describe the resonant loss feature using a model with coupled modes that is analogous to a Fabry–Pérot cavity. Our observations provide strong evidence for the existence of long-lived coherent intermediate complexes even in systems without reaction barriers and open up the possibility of coherent control of chemical reactions.

Collisional resonances profoundly change the properties of ultracold gases. Magnetically tunable Feshbach resonances have been used to modify interactions between ultracold atoms from strong to weak and attractive to repulsive, as well as to coherently convert atomic gases into molecular gases<sup>2</sup>. Collisional resonances have become an important tool not only for creating previously unknown Hamiltonians in quantum simulations<sup>1</sup> but also for investigating and understanding interatomic potentials and interactions.

It has been a long-standing goal for the field of ultracold molecules to harness the power of collisional resonances. Ultracold molecules provide opportunities to study quantum-state-controlled chemistry<sup>16,17</sup>, quantum simulation<sup>18–20</sup> and quantum information processing<sup>21–24</sup>. Recent progress in the production of ultracold molecules from ultracold atoms<sup>25–31</sup> or direct laser cooling of molecules<sup>32,33</sup> has laid the groundwork for achieving atom-like control of ultracold molecules.

For molecular systems, collisional resonances can provide microscopic information about collision complexes and they can be used to alter chemical reactions. However, Feshbach resonances have previously been observed only in two systems of atom–molecule collisions (NaK + K (refs. <sup>3,4</sup>) and NaLi + Na (ref. <sup>5</sup>)) and for collisions involving Feshbach molecules, which are vibrationally excited molecules close to the dissociation continuum with resonances close to atomic Feshbach resonances<sup>6–10</sup>. It has even been an open question as to whether

collisional resonances can be observed at all for ultracold, tightly bound molecules owing to the high density of states and rapid decay of resonant states<sup>11–15</sup>.

We report the observation of a pronounced, isolated Feshbach resonance in collisions between fermionic NaLi molecules in their triplet rovibronic ground state. The magnetically tunable resonance is extremely narrow (about 25 mG) and enhances the loss rate by more than two orders of magnitude, providing strong evidence for a stable, long-lived collision complex. The existence of long-lived complexes in a molecular system of high reactivity such as NaLi + NaLi is unexpected and has strong implications for controlling ultracold chemistry through scattering resonances. The long-lived state shown by our experiments is coherently excited, whereas all other observations of collisional complexes in molecule–molecule collisions<sup>34–39</sup> are compatible with an incoherent population.

The observed resonance is special in two regards. In simple models, resonantly enhanced losses are only possible if the background loss rate is much lower than the so-called universal limit<sup>40</sup>. A loss rate near the universal limit implies almost complete inelastic loss at short range and should suppress any long-lived resonant state. However, we observe loss rates close to the universal limit outside the narrow resonance. Second, the NaLi + NaLi Feshbach resonance is observed at a specific magnetic field where two open channels become degenerate. It is possibly a new

<sup>1</sup>MIT-Harvard Center for Ultracold Atoms, Research Laboratory of Electronics, Department of Physics, Massachusetts Institute of Technology, Cambridge, MA, USA. <sup>2</sup>Institute for Quantum Computing, University of Waterloo, Waterloo, Ontario, Canada. <sup>3</sup>Department of Physics and Astronomy, University of Waterloo, Waterloo, Ontario, Canada. <sup>4</sup>Department of Physics, University of Nevada, Reno, NV, USA.  e-mail: jjpark@mit.edu

type of Feshbach resonance with a mechanism different from those observed so far in ultracold atomic systems. This mechanism cannot be realized in ultracold collisions of alkali-metal atoms because the required single-particle-level degeneracies do not occur at practicable field strengths. By contrast, degeneracies between two-particle threshold energies are commonly found in molecule–molecule collisions and have been used to engineer shielding interactions in ultracold KRb + KRb and CaF + CaF collisions<sup>41–43</sup>. Our results indicate that this new type of degeneracy-induced magnetic resonance could be ubiquitous in ultracold molecular physics, offering a powerful new mechanism for tuning intermolecular interactions with external electromagnetic fields. We explain the observed behaviour with simple models.

The experiment is carried out with  $^{23}\text{Na}^6\text{Li}(a^3\Sigma^+)$  molecules in the rovibrational triplet ground state. The molecules are prepared with all spins aligned in the lower stretched hyperfine state. Following the techniques described in ref.<sup>5</sup>, we prepare  $6 \times 10^4$  molecules at  $1.8 \mu\text{K}$  in a 1,596-nm 1D optical lattice potential (further details in Methods). We coarsely search for resonant loss by sweeping the bias field in 600 ms by 3 G in steps of 2 G. Any loss feature in the 3-G range will show up as a reduced molecule number at the end of the sweep. Only one feature was observed in the range  $40.5 \text{ G} < B < 1,401.6 \text{ G}$ . By performing finer scans around this loss feature, the Feshbach resonance was identified to have a width of 25 mG centred at 334.92 G (Fig. 1a). The molecules become almost completely depleted at this field in 50 ms, whereas more than half of the molecules survive at the background after 1 s, as shown in Fig. 1b. We show that the losses are due to two-body *p*-wave collisions by investigating the density and temperature dependences of the decay rate.

To characterize the loss mechanism, the molecular decay rate,  $R_o$ , is measured as a function of the initial density,  $n_o$ , and compared with the behaviour  $\beta n_o^{(y-1)}$  expected for decay by collisions involving  $\gamma$  particles. A power-law fit gives  $y = 1.85(9)$ , which confirms that the observed decay is due to binary collisions. Next, we map out the temperature dependence of the molecular decay rate constant and compare with the Wigner threshold law<sup>44</sup>. We generate molecular gases at different temperatures by varying the initial temperature of the Na/Li atomic mixture. The observed decay rate depends linearly on temperature, as expected from the *p*-wave Wigner threshold law<sup>44</sup> for collisions between two identical fermions (see Methods for the characterization of the decay in detail).

Natural comparisons for the observed decay rates are the universal limit and the unitarity limit. The universal limit assumes perfect absorption of scattering flux at short range and is given by  $\beta_{l=1}^{\text{univ.}} = 1,513 \bar{a}^3 \frac{k_B T}{h} = 1.2 \times 10^{-12} (\text{cm}^3 \text{s}^{-1}) (T_{\text{NaLi}}/1 \mu\text{K})$  for identical NaLi *p*-wave collisions, in which  $\bar{a} = 4\pi R_{\text{vdW}}/\Gamma\left(\frac{1}{4}\right)$ , with the van der Waals (vdW) length  $R_{\text{vdW}} = \frac{1}{2} \left( \frac{2\mu C_6}{h^2} \right)^{1/4} \approx 66 a_0$  (ref.<sup>40</sup>). Here  $\mu = m_{\text{NaLi}}/2$  is the reduced mass and we use an approximate value of the NaLi–NaLi long-range dispersion coefficient ( $C_6 = 5,879$  a.u.) obtained by summing all  $C_6$  coefficients between the two constituent atoms<sup>45</sup>. When reflected flux at close/short range destructively interferes with the reflected flux at long range, loss rates can exceed the universal limit but are always limited by the unitarity limit<sup>46</sup>. Our experiments in a 1D optical lattice are carried out in the crossover between 2D and 3D physics. For a quasi-2D trap, the unitarity limit is given by  $\beta_{2D}^{\text{unit.}} = 4 \frac{\hbar}{\mu} (\sqrt{\pi} l_0)$  (ref.<sup>47</sup>). We see that  $\beta_{2D}^{\text{unit.}}$  scales linearly with the oscillator length in the tightly confined direction,  $l_0 = (\hbar/m_{\text{NaLi}}\omega_z)^{1/2}$ . By contrast, the 3D unitarity limit neglects the zero-point motion owing to 2D confinement and is given by  $\beta_{3D}^{\text{unit.}} = 6 \frac{\hbar}{\mu} \lambda_{\text{dB}}$ , in which  $\lambda_{\text{dB}}$  is the thermal de Broglie wavelength  $\lambda_{\text{dB}} = \sqrt{2\pi\hbar^2/k_B\mu T}$ . Our experiments were carried out in the regime in which the zero-point energy is larger than the thermal energy, and rates should be limited by the 2D limit because the 3D unitarity limit is higher.

The background loss-rate constants (at 745 G) were obtained for various molecule temperatures and estimated to be  $1.7(5) \times 10^{-12} (\text{cm}^3 \text{s}^{-1}) (T_{\text{NaLi}}/1 \mu\text{K})$  from a linear fit. This background loss-rate constant matches the *p*-wave universal value within the uncertainty. The rate constant,  $\beta$ , increases by more than two orders of magnitude as the bias field

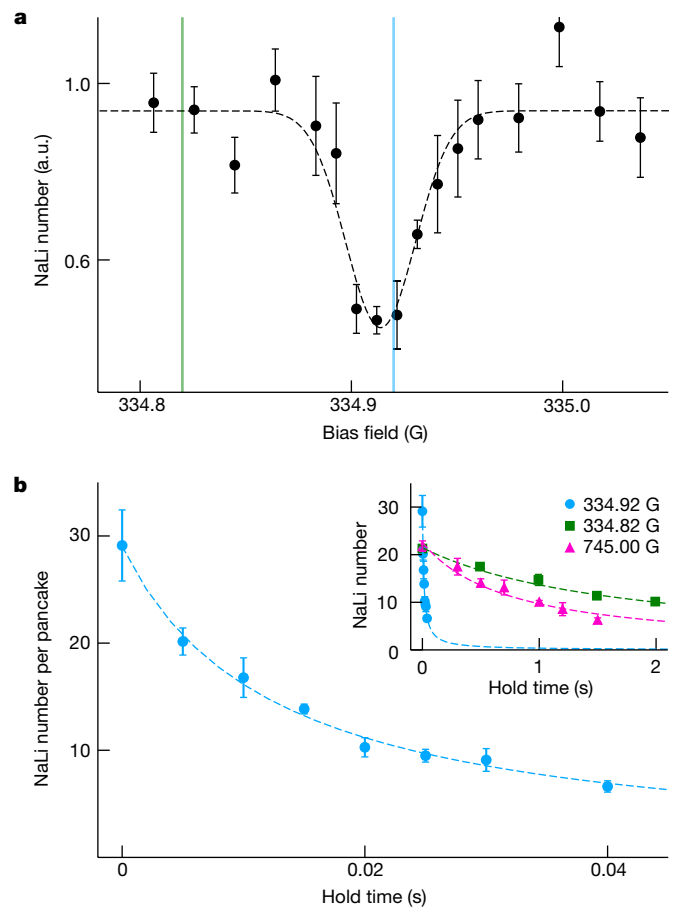


**Fig. 1 | Resonant molecular loss.** **a**, The remaining molecule number after holding for 30 ms at a target field is mapped out for various magnetic fields near 334.9 G. Molecule numbers are normalized by the number without the hold. Each data point represents three to six measurements with and without 30-ms hold and the error bars are one standard deviation. The dashed black line is a Gaussian fit. The vertical blue (green) line indicates the field in which the molecular decay curve in blue (green) is obtained in **b**. **b**, The main plot shows the decay curve near the centre of the resonance (334.92 G) within 50 ms. The inset shows decay curves away from the resonance at 334.82 G (green squares), at 745.00 G (red triangles) and at 334.92 G (blue circles) over 2 s. Dashed lines are fits to a simple model for two-body loss using mean square regression (see Methods for details). Data values represent the average and error bars represent one standard deviation of the mean, estimated from statistical errors of three to six measurements.

approaches 334.918(5) G from near the *p*-wave universal value to above the *s*-wave universal value. Loss-rate coefficients are plotted as a function of magnetic field and fitted to a Lorentzian function for two temperatures,  $1.8 \mu\text{K}$  and  $4.2 \mu\text{K}$ , in Fig. 2. The loss-rate-constant contrast is  $\approx 150$  for  $1.8 \mu\text{K}$  and  $\approx 230$  for  $4.2 \mu\text{K}$ . The rate constants at the peaks are below the 3D unitarity limits but approach the 2D unitarity limits. The width of the resonance is comparable with the inhomogeneity of the magnetic field across the molecular sample,  $\approx 25$  mG. Lorentzian widths from the fits for both  $1.8 \mu\text{K}$  and  $4.2 \mu\text{K}$  are also  $\approx 25$  mG and are probably broadened by the field inhomogeneity. The result at  $4.2 \mu\text{K}$  shows an overall higher loss-rate constant compared with that of  $1.8 \mu\text{K}$ , as expected from the *p*-wave threshold law at the resonance,  $\beta \propto T$ , mentioned earlier.

We now develop a model that addresses our main experimental findings. The universal limit assumes that the loss rate is given by all the flux that has not been quantum reflected, that is, has tunneled through the centrifugal barrier located at  $\approx 2.2R_{\text{vdW}}$ . Rates higher than the universal limit as observed here are only possible if the losses occur at long range (outside the *p*-wave barrier) or if substantial back reflection

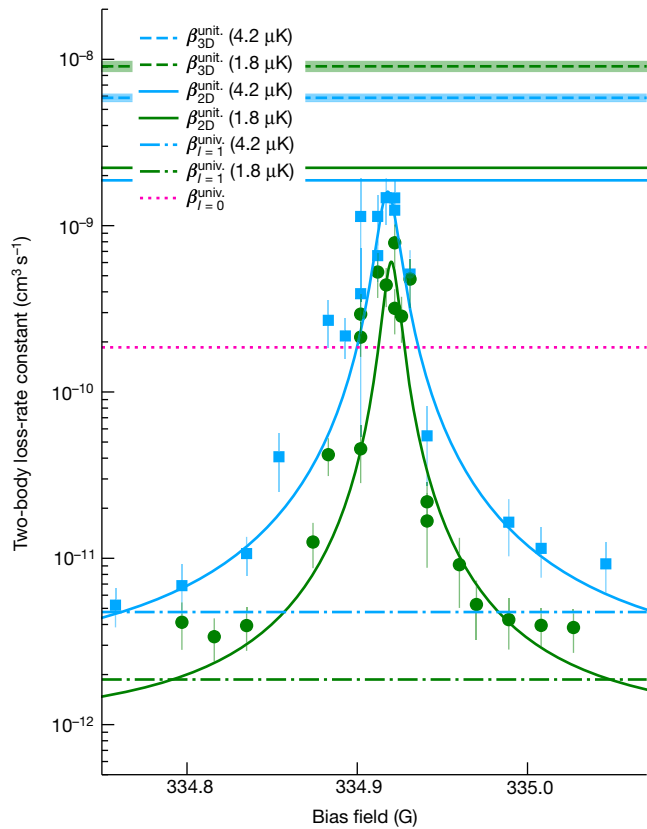


**Fig. 2 | Two-body loss-rate coefficient.** The initial two-body loss-rate coefficients are plotted as a function of the bias field for initial temperatures  $\approx 4.2 \mu\text{K}$  (blue squares) and  $\approx 1.8 \mu\text{K}$  (green circles). Data points were obtained using a simple two-body loss model (see Methods) from five to eight different hold times at each bias field; three to six measurements at a given hold time were averaged. Error bars represent one standard deviation of a fitted decay parameter. Solid lines are Lorentzian fits. The dotted red line is the s-wave universal value for distinguishable NaLi  $\beta_{l=0}^{\text{univ.}} = 2 \frac{\hbar}{\mu} \bar{a} = 1.85 \times 10^{-10} \text{ cm}^3 \text{ s}^{-1}$  and dash-dot lines are p-wave universal values  $\beta_{l=1}^{\text{univ.}} = 1, 513 \bar{a}^3 \frac{k_B T}{\hbar} = 1.2 \times 10^{-12} (\text{cm}^3 \text{ s}^{-1}) (T_{\text{NaLi}}/1 \mu\text{K})$  for  $T = 4.2 \mu\text{K}$  (blue) and  $T = 1.8 \mu\text{K}$  (green). The dashed horizontal lines are the 3D unitarity limits and the solid horizontal lines are the 2D unitarity limits.

from behind the centrifugal barrier destructively interferes with the reflection at long range. Spin-flip processes can, in principle, happen at long range owing to the magnetic dipole–dipole interaction, but for the nearly degenerate hyperfine states in our system (see Methods for the hyperfine structure of NaLi), the quantum numbers for the  $z$ -component of the electron spin differ by two from the input channel, so coupling by single spin flips is forbidden. Higher-order spin flips owing to the intramolecular spin–spin and spin–rotation couplings are too weak: a loss-rate constant greater than  $10^{-10} \text{ cm}^3 \text{ s}^{-1}$  requires a coupling strength on the order of 16 kHz at long range (about 100 nm). However, the strongest higher-order process has a coupling strength of around 0.05 kHz (further details in Methods). We therefore assume that we have a  $p$ -wave resonance enabled by high reflectivity at close range.

In principle, the observed resonance could be an ordinary  $p$ -wave resonance. However, the fact that this resonance occurs exactly at the magnetic field where the input channel becomes degenerate with another open channel suggests a new mechanism for which we introduce a minimal model. This model assumes two nearly degenerate states,  $|1\rangle$  and  $|2\rangle$ , coupled to a quasi-bound state,  $|3\rangle$ , in which two molecules are held together by the  $p$ -wave barrier and reflection at short range (see Fig. 3a). The transferred flux from the incoming flux  $I$  in state  $|1\rangle$  to state  $|2\rangle$  depends on the coupling strengths  $\gamma_i$  between channel  $|3\rangle$  and the open channels  $|1\rangle$  and  $|2\rangle$  and on the energy difference between the incoming state  $\hbar\omega$  and the quasi-bound state  $\hbar\omega_0$ :

$$T_{\text{trans}} = I \cdot \frac{\gamma_1 \gamma_2}{(\omega_0 - \omega)^2 + [(\gamma_1 + \gamma_2)/2]^2}. \quad (1)$$

The process is fully analogous to a harmonic oscillator with resonance  $\omega_0$  and damping rate  $\gamma_2$  driven at frequency  $\omega$  by means of a frictional input coupling  $\gamma_1$ . The power dissipated through  $\gamma_2$  (normalized to a quarter of the drive power at zero amplitude of the harmonic oscillator) is exactly given by equation (1) (see Methods for details).

It is even more intuitive to generalize the optical analogue we developed in a previous paper<sup>5</sup>, which treated long-range quantum reflection and reflection at short range as the two mirrors of a Fabry–Pérot interferometer. In our optical analogue, the coupling to the second open channel is represented by transmission through the inner mirror, as shown in Fig. 3b. In the simplest model, we assume no further loss for state 3 at short range.

Tuning the coupling term,  $\gamma_2$ , now leads to a pronounced resonance-type feature in the Fabry–Pérot transmission. For small  $\gamma_2$ , transmission is proportional to  $\gamma_2$ . However, for large  $\gamma_2$ , the quality factor of the resonance is reduced, there is less and less build-up of light inside the resonator and the transmission decreases with  $\gamma_2$ . For resonant coupling ( $\omega - \omega_0 \ll \gamma_1$ ), the maximum transmission is 100% ( $T_{\text{trans}} = I$ ) when  $\gamma_2 = \gamma_1$ , whereas for off-resonant coupling ( $\omega - \omega_0 \gg \gamma_1$ ), the maximum transmission is at the reduced value of  $\gamma_1/(\omega - \omega_0)$  when  $\gamma_2 = 2(\omega - \omega_0)$ , as shown in Fig. 3c.

We are using a generalization of the model from ref. <sup>48</sup> in the treatment of atomic  $p$ -wave Feshbach resonances, which can be used to connect the parameters in equation (1) to a microscopic scattering theory (see Methods for details). The scaling of  $\gamma_2$  comes from the threshold behaviour of  $p$ -wave inelastic collision rates ( $\propto k^2$ ) and the density of states of an open channel ( $\propto k'$ ). When the external magnetic field is lowered, it tunes channel  $|2\rangle$  from above to below the energy of the input channel  $|1\rangle$ . Initially, channel  $|2\rangle$  is closed. When it opens, it has zero coupling strength owing to the  $k^3$  term. For a magnetic field  $\Delta B$  below the threshold, the coupling strength grows  $\propto \Delta B^{3/2}$ , which tunes the loss across its maximum, as in Fig. 3c.

Using a similar scaling for  $\gamma_1 \propto k^3$ , in which  $k$  is the wavevector in the input channel  $|1\rangle$ , we obtain the inelastic loss rate:

$$g_2 \propto \frac{k^{-1} \gamma_1 \gamma_2}{(E - E_0)^2 + [(\gamma_1 + \gamma_2)/2]^2}, \quad (2)$$

in which  $E$  is the incident energy and  $E_0$  is the resonant energy. In Methods, equation (2) is derived using a  $T$ -matrix formalism. Note that the numerator scales with  $k^2$  instead of  $k^3$ , which is different in structure from equation (1). The reason is that, for particle collisions, the initial channel has a specific wavevector, so we see threshold  $p$ -wave scaling ( $k^2$ ) for the input coupling. Inelastic decay from the closed channel proceeds into a continuum of states, which adds another power of  $k$  for the density of states in the continuum. The experimentally observed  $k^2$  dependence of the loss-rate constant implies that  $\gamma_1$  never dominates the other terms in the denominator of  $g_2$ . Derivation of equation (2) and the more general formalism including an extra loss channel for state 3 at short range are included in Methods.

We suggest that this mechanism is responsible for the observed resonance. For this, we assume that the incoming channel couples to a long-lived collision complex independent of the applied magnetic field, which would be the case for identical or similar magnetic moments in the two states. The magnetic field tunes the coupling to a second, nearly degenerate open channel. This may seem to call for a remarkable coincidence, but molecule–molecule collisions are predicted to have a high density of resonances<sup>11–14</sup>, so it is reasonable to assume that a near-threshold  $p$ -wave bound state is readily available at almost any magnetic field and collision energy.

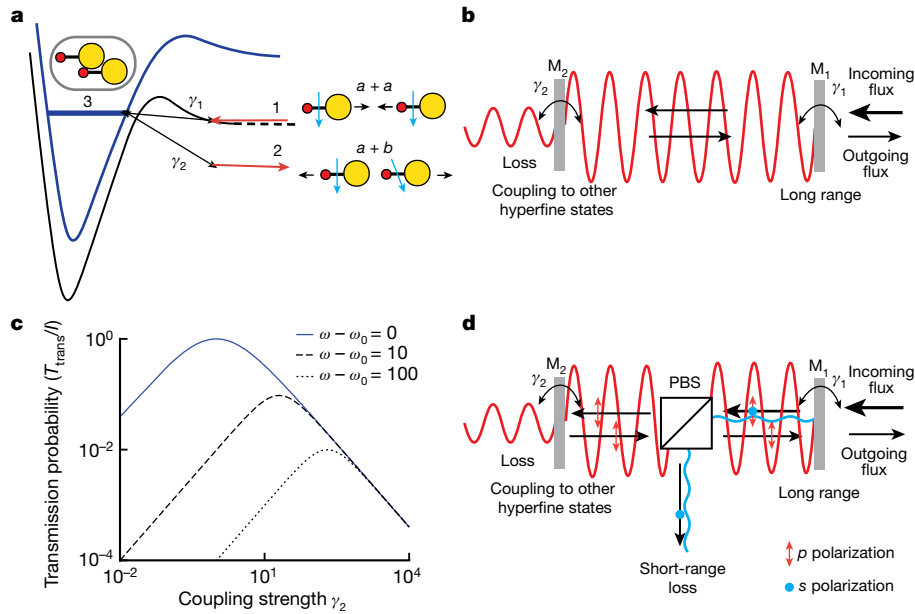


**Fig. 3 | Three-state model for the resonance and optical analogues.**

**a**, Schematic of the resonance model with two open channels and a *p*-wave bound state trapped behind a centrifugal barrier. Channels  $|1\rangle$  and  $|2\rangle$  are the open channels coupled to a closed channel  $|3\rangle$ . Channel  $|1\rangle$  corresponds to the initial scattering channel with two NaLi molecules in the lower stretched hyperfine state. Channel  $|2\rangle$  corresponds to another open channel in which molecules are in a different hyperfine state energetically close to the incident scattering state. **b**, Fabry-Pérot cavity model for molecular collisions. Two mirrors  $M_1$  and  $M_2$  couple light into and out of the Fabry-Pérot resonator created by these mirrors with coupling strengths  $\gamma_i$ . When the spacing between the mirrors is tuned to form a cavity mode resonant to the incoming light,

transmission loss is enhanced by constructive interference of light amplitudes inside the cavity. **c**, Transmission probability of a cavity as a function of mirror coupling strengths. For given coupling strength of the first mirror,  $\gamma_1$  (in arbitrary units), the transmission probability reaches unity for resonant coupling (blue line) at  $\gamma_2 = \gamma_1$  but maximizes to  $\gamma_1/(\omega - \omega_0)$  for far off-resonant coupling (black lines) at  $\gamma_2 = 2(\omega - \omega_0)$ . **d**, Schematic of a Fabry-Pérot cavity with a polarizing beam splitter (PBS). Two mirrors form a resonator at which the *p*-polarization component of the light amplitude is enhanced near a resonance. There are two paths for light to travel that are decoupled by the beam splitter. The *s*-polarization component is reflected by the PBS and lost from the cavity.

The model presented so far can explain a resonant enhancement of the loss as a function of magnetic field, but an enhancement by a factor of  $1/y$  would lead to an off-resonant suppression of loss below the universal limit by a factor of  $y$  on the basis of the results of the quantum defect model<sup>5,40</sup> ( $y$  is the standard short-range absorption parameter). However, we observe a background loss comparable with the universal loss rate. One possible explanation is that the incoming flux is split into two or more (orthogonal) components: one part has the resonant behaviour described above whereas the other part has non-resonant universal loss (that is, full transmission at short range). For example, if one-tenth of the scattering flux is coupled to the resonance, but its loss is enhanced by a factor of 1,000, the total loss can be 100 times the universal limit. Outside the resonance, most of the flux (assumed here to be 90%) provides the background loss near the universal rate. The optical analogy for this is the addition of a polarizing beam splitter to the Fabry-Pérot interferometer, shown in Fig. 3d. If most of the incoming flux matches the polarization that is reflected out of the cavity by the beam splitter, we would see a large background loss rate. Actually, for this polarization, we have the optical analogue of the universal limit at which the ‘inner mirror’ is absent owing to rapid short-range loss. If the molecule–molecule collision follows several paths split by some internal-state quantum numbers, this can explain the peculiarity of a large resonant enhancement above the universal limit from a background near the universal limit.

We estimate the lifetime of the complex using the analogy with the photon lifetime in a cavity, that is, the round-trip time multiplied by the resonant enhancement divided by 4. Using the observed loss-enhancement factor of 230, we obtain an estimated lifetime of 320 ns. We regard this as a low estimate. Even if the *p*-wave resonance is at resonance, owing to thermal broadening, the maximum loss enhancement is reduced by a factor  $\hbar y_i/k_B T$ . For a collision energy of

4.2  $\mu$ K, the reduction factor is approximately 0.1, which implies a ten times larger lifetime. Furthermore, if we assume that the loss enhancement is possibly not 230 but 2,300 for 10% of the incident flux (model with polarization beam splitter), then the lifetime would be another factor of ten higher and could be tens of microseconds. The observed enhancement of 230 provides an upper bound for the short-range absorption coefficient  $y \leq 0.0043$  (see Methods for details).

The most surprising aspect of our results is the existence of a long-lived collision complex in NaLi + NaLi collisions, which allow barrier-free chemical reactions in all channels<sup>49</sup>. A long-lived complex is necessary for the existence of a high-Q resonance, such as we have observed, independently of any detailed model. Our observation of resonant behaviour is very different from other recent experiments reporting long-lived collision complexes in molecule–molecule collisions, observed by means of photoionization<sup>34</sup> or inferred as the source of optical trap loss<sup>35–39</sup>. These observations were fitted to rate equations and are most probably related to ‘sticky’ collisions<sup>11–15</sup> connected with a high density of states. Such complexes are formed incoherently and lead to loss at the universal rate. By contrast, an enhancement above the universal rate (as observed here) is only possible when the flux reflected at short range destructively interferes with the quantum-reflected flux and, therefore, requires full phase coherence.

In summary, we report an unexpected new type of Feshbach resonance in ultracold molecule–molecule collisions, the first observed between rovibrational ground-state molecules at ultracold temperatures. The resonance arises from a background loss at the universal limit, which is impossible with the most commonly studied models of ultracold collisions. The observed more than hundredfold enhancement of loss implies the existence of a remarkably long-lived collision complex in a system with barrier-free reactions in all channels. The observed resonance could be an ordinary *p*-wave resonance.

However, we propose a more plausible mechanism that operates near a single-molecule degeneracy. This suggests that one should look for new collisional properties near known degeneracies in other molecular systems focusing on points with sufficient nuclear spin overlap.

Although we explain the unusual features with a phenomenological model, they raise many questions for future work. Are narrow resonances such as ours unique to molecules with light atoms and therefore a lower density of states? Are resonant quasibound states coexisting with lossy channels a common feature of molecular systems that has so far gone undetected? In our case, we could detect the quasibound state only by modifying the coupling to a second, nearly degenerate open channel, and it is possible that many more long-lived states exist at other magnetic-field values. Resonant states with low loss should have a distinct signature on elastic-scattering properties, which, however, may be difficult to measure in the presence of strong loss. Or does the non-observation of any other magnetically tunable molecule–molecule Feshbach resonance imply that those resonances are, in general, very dense, or broadened by strong coupling to other states or decay channels, and therefore not resolved? Our and other recent results<sup>35–39</sup> emphasize that the properties of collision complexes—even for the simplest molecular systems—are far from being understood.

## Online content

Any methods, additional references, Nature Portfolio reporting summaries, source data, extended data, supplementary information, acknowledgements, peer review information; details of author contributions and competing interests; and statements of data and code availability are available at <https://doi.org/10.1038/s41586-022-05635-8>.

1. Bloch, I., Dalibard, J. & Nascimbene, S. Quantum simulations with ultracold quantum gases. *Nat. Phys.* **8**, 267–276 (2012).
2. Chin, C., Grimm, R., Julienne, P. & Tiesinga, E. Feshbach resonances in ultracold gases. *Rev. Mod. Phys.* **82**, 1225 (2010).
3. Yang, H. et al. Observation of magnetically tunable Feshbach resonances in ultracold  $^{23}\text{Na}^{40}\text{K} + ^{40}\text{K}$  collisions. *Science* **363**, 261–264 (2019).
4. Wang, X.-Y. et al. Magnetic Feshbach resonances in collisions of  $^{23}\text{Na}^{40}\text{K}$  with  $^{40}\text{K}$ . *New J. Phys.* **23**, 115010 (2021).
5. Son, H. et al. Control of reactive collisions by quantum interference. *Science* **375**, 1006–1010 (2022).
6. Knoop, S. et al. Observation of an Efimov-like trimer resonance in ultracold atom–dimer scattering. *Nat. Phys.* **5**, 227–230 (2009).
7. Zenesini, A. et al. Resonant atom–dimer collisions in cesium: testing universality at positive scattering lengths. *Phys. Rev. A* **90**, 022704 (2014).
8. Chin, C. et al. Observation of Feshbach-like resonances in collisions between ultracold molecules. *Phys. Rev. Lett.* **94**, 123201 (2005).
9. Wang, F., Ye, X., Guo, M., Blume, D. & Wang, D. Observation of resonant scattering between ultracold heteronuclear Feshbach molecules. *Phys. Rev. A* **100**, 042706 (2019).
10. Ferlaino, F. et al. Collisions of ultracold trapped cesium Feshbach molecules. *Laser Phys.* **20**, 23–31 (2010).
11. Mayle, M., Ruzic, B. P. & Bohn, J. L. Statistical aspects of ultracold resonant scattering. *Phys. Rev. A* **85**, 062712 (2012).
12. Mayle, M., Quéméner, G., Ruzic, B. P. & Bohn, J. L. Scattering of ultracold molecules in the highly resonant regime. *Phys. Rev. A* **87**, 012709 (2013).
13. Christianen, A., Karman, T. & Groenenboom, G. C. Quasiclassical method for calculating the density of states of ultracold collision complexes. *Phys. Rev. A* **100**, 032708 (2019).
14. Christianen, A., Zwierlein, M. W., Groenenboom, G. C. & Karman, T. Photoinduced two-body loss of ultracold molecules. *Phys. Rev. Lett.* **123**, 123402 (2019).
15. Liu, Y. & Ni, K.-K. Bimolecular chemistry in the ultracold regime. *Annu. Rev. Phys. Chem.* **73**, 73–96 (2022).
16. Krems, R. V. Cold controlled chemistry. *Phys. Chem. Chem. Phys.* **10**, 4079–4092 (2008).
17. Balakrishnan, N. Perspective: Ultracold molecules and the dawn of cold controlled chemistry. *J. Chem. Phys.* **145**, 150901 (2016).
18. Micheli, A., Brennen, G. & Zoller, P. A toolbox for lattice-spin models with polar molecules. *Nat. Phys.* **2**, 341–347 (2006).
19. Capogrosso-Sansone, B., Trefzger, C., Lewenstein, M., Zoller, P. & Pupillo, G. Quantum phases of cold polar molecules in 2D optical lattices. *Phys. Rev. Lett.* **104**, 125301 (2010).
20. Blackmore, J. A. et al. Ultracold molecules for quantum simulation: rotational coherences in CaF and RbCs. *Quantum Sci. Technol.* **4**, 014010 (2018).
21. Ni, K.-K., Rosenband, T. & Grimes, D. D. Dipolar exchange quantum logic gate with polar molecules. *Chem. Sci.* **9**, 6830–6838 (2018).
22. Herrera, F., Cao, Y., Kais, S. & Whaley, K. B. Infrared-dressed entanglement of cold open-shell polar molecules for universal matchgate quantum computing. *New J. Phys.* **16**, 075001 (2014).
23. Hughes, M. et al. Robust entangling gate for polar molecules using magnetic and microwave fields. *Phys. Rev. A* **101**, 062308 (2020).
24. Sawant, R. et al. Ultracold polar molecules as qudits. *New J. Phys.* **22**, 013027 (2020).
25. Rvachov, T. M. et al. Long-lived ultracold molecules with electric and magnetic dipole moments. *Phys. Rev. Lett.* **119**, 143001 (2017).
26. Ni, K.-K. et al. A high phase-space-density gas of polar molecules. *Science* **322**, 231–235 (2008).
27. Winkler, K., Lang, F., Thalhammer, G., vd Straten, P., Grimm, R. & Denschlag, J. H. Coherent optical transfer of Feshbach molecules to a lower vibrational state. *Phys. Rev. Lett.* **98**, 043201 (2007).
28. Danzl, J. G. et al. An ultracold high-density sample of rovibronic ground-state molecules in an optical lattice. *Nat. Phys.* **6**, 265–270 (2010).
29. Park, J. W., Will, S. A. & Zwierlein, M. W. Ultracold dipolar gas of fermionic  $\text{Na}^{23}\text{K}^{40}$  molecules in their absolute ground state. *Phys. Rev. Lett.* **114**, 205302 (2015).
30. Danzl, J. G. et al. Quantum gas of deeply bound ground state molecules. *Science* **321**, 1062–1066 (2008).
31. Krzyzewski, S. P., Akin, T. G., Dizikes, J., Morrison, M. A. & Abraham, E. R. I. Observation of deeply bound  $^{85}\text{Rb}_2$  vibrational levels using Feshbach optimized photoassociation. *Phys. Rev. A* **92**, 062714 (2015).
32. Shuman, E. S., Barry, J. F. & DeMille, D. Laser cooling of a diatomic molecule. *Nature* **467**, 820–823 (2010).
33. Anderegg, L. et al. Laser cooling of optically trapped molecules. *Nat. Phys.* **14**, 890–893 (2018).
34. Hu, M.-G. et al. Direct observation of bimolecular reactions of ultracold KRb molecules. *Science* **366**, 1111–1115 (2019).
35. Liu, Y. et al. Photo-excitation of long-lived transient intermediates in ultracold reactions. *Nat. Phys.* **16**, 1132–1136 (2020).
36. Gregory, P., Blackmore, J., Bromley, S. & Cornish, S. Loss of ultracold  $^{87}\text{Rb}^{133}\text{Cs}$  molecules via optical excitation of long-lived two-body collision complexes. *Phys. Rev. Lett.* **124**, 163402 (2020).
37. Gregory, P. D. et al. Molecule–molecule and atom–molecule collisions with ultracold RbCs molecules. *New J. Phys.* **23**, 125004 (2021).
38. Gersema, P. et al. Probing photoinduced two-body loss of ultracold nonreactive bosonic  $^{23}\text{Na}^{87}\text{Rb}$  and  $^{23}\text{Na}^{39}\text{K}$  molecules. *Phys. Rev. Lett.* **127**, 163401 (2021).
39. Bause, R. et al. Collisions of ultracold molecules in bright and dark optical dipole traps. *Phys. Rev. Res.* **3**, 033013 (2021).
40. Idziaszek, Z. & Julienne, P. S. Universal rate constants for reactive collisions of ultracold molecules. *Phys. Rev. Lett.* **104**, 113202 (2010).
41. Matsuda, K. et al. Resonant collisional shielding of reactive molecules using electric fields. *Science* **370**, 1324–1327 (2020).
42. Schindewolf, A. et al. Evaporation of microwave-shielded polar molecules to quantum degeneracy. *Nature* **607**, 677–681 (2022).
43. Anderegg, L. et al. Observation of microwave shielding of ultracold molecules. *Science* **373**, 779–782 (2021).
44. Wigner, E. P. On the behavior of cross sections near thresholds. *Phys. Rev.* **73**, 1002 (1948).
45. Derevianko, A., Babb, J. & Dalgarno, A. High-precision calculations of van der Waals coefficients for heteronuclear alkali–metal dimers. *Phys. Rev. A* **63**, 052704 (2001).
46. Julienne, P. S., Hanna, T. M. & Idziaszek, Z. Universal ultracold collision rates for polar molecules of two alkali–metal atoms. *Phys. Chem. Chem. Phys.* **13**, 19114–19124 (2011).
47. Idziaszek, Z., Jachymski, K. & Julienne, P. S. Reactive collisions in confined geometries. *New J. Phys.* **17**, 035007 (2015).
48. Chevy, F. et al. Resonant scattering properties close to a p-wave Feshbach resonance. *Phys. Rev. A* **71**, 062710 (2005).
49. Tomza, M., Madison, K. W., Moszynski, R. & Krems, R. V. Chemical reactions of ultracold alkali–metal dimers in the lowest-energy  $^3\Sigma$  state. *Phys. Rev. A* **88**, 050701 (2013).

**Publisher's note** Springer Nature remains neutral with regard to jurisdictional claims in published maps and institutional affiliations.

Springer Nature or its licensor (e.g. a society or other partner) holds exclusive rights to this article under a publishing agreement with the author(s) or other rightsholder(s); author self-archiving of the accepted manuscript version of this article is solely governed by the terms of such publishing agreement and applicable law.

© The Author(s), under exclusive licence to Springer Nature Limited 2023

## Methods

### Experimental sequence

Our experiments use ground-state  $^{23}\text{Na}^6\text{Li}(a^3\Sigma^+)$  molecules in their lower stretched hyperfine state ( $|F, M_F\rangle = |7/2, -7/2\rangle$ ), in which all nuclear and electron spins are anti-aligned to the bias magnetic field direction, trapped in a 1D optical lattice made with 1,596-nm light. As described previously<sup>5,25,50</sup>, we first produce loosely bound molecules through magnetic association at a Feshbach resonance near 745 G, followed by stimulated Raman adiabatic passage to the rovibrational ground state. These triplet ground-state molecules are in the upper stretched hyperfine state ( $|F, M_F\rangle = |7/2, 7/2\rangle$ ). The bias field is reduced from 745 G to a low field near 8 G in 15 ms, at which a magnetic-field sweep in the presence of radiofrequency waves coherently transfers them from the upper stretched state to the lower stretched state.

After state preparation, the magnetic field is ramped to a target value in 15 ms. A search for scattering resonances is done for the bias field range of  $40.5 \text{ G} < B < 1,401.6 \text{ G}$ . After waiting a certain time for the molecules to collide with one another at the target field, we reduce the field back to 8 G for reverse state transfer ( $|7/2, -7/2\rangle \rightarrow |7/2, 7/2\rangle$ ). The field is raised back to 745 G, at which the molecules are dissociated. We use absorption imaging of the resulting lithium atoms to measure molecule number and temperature. A hold time of 15 ms  $< t < 30$  ms after each magnetic-field ramp was sufficient for the bias field to settle within the range of the magnetic-field inhomogeneity across the molecular sample.

### Characterization of the decay

We investigate the effect of impurities to confirm that the enhanced loss near 334.92 G is due to collisions between fermionic molecules in a single state. A small amount of impurities owing to imperfect state preparation could cause rapid initial decay resulting from *s*-wave collisions that are not suppressed by Pauli exclusion. However, after a rapid loss of these impurities, the fast decay would stop. By observing almost full decay of the molecular sample, we rule out that the fast decay is related to impurities. Figure 1b shows that about 30 molecules per lattice site decay to approximately seven molecules in 40 ms and are depleted to a barely detectable level in less than 100 ms.

Furthermore, the density dependence and the temperature dependence of the decay rate shown in Extended Data Fig. 1 prove that the loss occurs owing to two-body collisions. The molecular decay rate,  $R_o$ , is measured as a function of the initial density,  $n_o$ , and compared with the behaviour  $\beta n_o^{(\gamma-1)}$  expected for decay by collisions involving  $\gamma$  particles. In general, the loss-rate constant  $\beta$  is dependent on temperature. To avoid a more complicated analysis, we controlled the initial temperatures of the molecules to be the same within 15%. Extended Data Fig. 1a shows that the observed decay is due to binary collisions (a power-law fit gives  $\gamma = 1.85(9)$ ). Next, the molecular decay rate constant,  $\beta(T)$ , is measured as a function of temperature. We generate molecular gases at different temperatures by varying the initial temperature of the Na/Li atomic mixture. Initial molecule temperatures ranging from  $0.74(8) \mu\text{K}$  to  $3.88(36) \mu\text{K}$  and from  $1.33(7) \mu\text{K}$  to  $4.40(25) \mu\text{K}$  are achieved away from (745 G) and at the resonance (334.92 G), respectively. The observed decay rate in Extended Data Fig. 1b depends linearly on temperature. A power-law fit  $\beta = CT^l$ , in which  $T$  is the temperature, results in  $l = 1.4(2)$  at the resonance and  $l = 0.98(19)$  at 745 G.

We model two-body loss with a differential equation that takes the time dependence of temperature into account<sup>51</sup>:

$$\dot{n}(t) = -\beta(T(t))n^2(t) - \frac{3}{2}n(t)\frac{\dot{T}(t)}{T(t)}, \quad (3)$$

in which  $\beta$  is the two-body loss-rate constant,  $n$  is the mean density and  $T$  is the temperature of the molecules. Molecules are lost preferentially from the highest density region. This ‘anti-evaporation’ causes

temperature increases of up to 50% within one molecular decay time near 334.9 G. We fit measured temperatures to a linear function of time,  $T(t) = Ht + T_o$ , in which  $H$  is the heating rate and  $T_o$  is the initial temperature. Both away from and near to the resonance, the loss-rate coefficient has a temperature dependence that can be expressed as  $\beta = \beta_0(T(t)/T_0)$ , in which  $\beta_0$  is the initial loss-rate coefficient when the temperature is  $T_0$ . To determine the rate coefficient from equation (3) requires accurate knowledge of the molecular density. The mean molecular density can be expressed with the effective number of particles,  $N^{\text{eff}}$ , and the mean volume,  $V_{\text{eff}}$ , of molecules for a single pancake as  $n = N^{\text{eff}}/V_{\text{eff}}$ .

We obtained the effective particle numbers for a single pancake from the measured number of molecules,  $N^{\text{tot}}$ , and the number distribution over pancakes. The observed axial profile of NaLi follows a Gaussian form with width  $\sigma = 450(60) \mu\text{m}$ , so we assume a Gaussian distribution of the particle number per pancake. As the average weighted over a Gaussian, the effective particle number per pancake is  $N^{\text{eff}} = N^{\text{tot}} \cdot a/(2\sqrt{\pi} \cdot \sigma)$ , in which the lattice constant  $a = \lambda/2$  and  $\lambda = 1,596 \text{ nm}$ .

The trap volume of each pancake,  $V_{\text{eff}}$ , is determined from the measured molecule temperature and trap frequencies. For a purely harmonic trap, one obtains  $V_{\text{eff}}^{(0)} = \bar{\omega}^{-3}(4\pi k_B T/m)^{3/2}$ , in which the geometric mean of the NaLi trap frequencies  $\bar{\omega} = (\omega_x \omega_y \omega_z)^{1/3}$ . However, there are two corrections that we determine separately: (1) the confinement in each pancake is moderately anharmonic and (2) the system is in the crossover regime between quasi-2D and 3D,  $k_B T \approx \hbar \omega_z$ .

First, the anharmonicity of the trapping potential leads to a modified mean volume  $V_{\text{eff}}^{(1)}$

$$1/V_{\text{eff}}^{(1)} = \frac{\int dV e^{-2\beta U(r,z)}}{\left[ \int dV e^{-\beta U(r,z)} \right]^2} \quad (4)$$

in which  $U(r, z)$  is the potential of a single lattice site,  $r$  is the radial coordinate,  $z$  is the axial coordinate along the beam direction and  $\beta = (k_B T)^{-1}$ . We use the same trap model validated in ref. <sup>5</sup> to determine  $U(r, z)$  and the same integration limits. With typical conditions for molecular loss measurements, the mean volume  $V_{\text{eff}}^{(1)}$  is larger than  $V_{\text{eff}}^{(0)}$  by less than 25%. However, some measurements at lower density required weaker optical traps, for which the anharmonicity correction is larger and had to be taken into account for proper density calibration.

Second, the tight confinement in the lattice direction makes the classical thermal distribution for harmonic trapping in the pancakes invalid for low molecular temperatures. We estimate the corrected volume as

$$1/V_{\text{eff}}^{(2)} = \frac{\int dV \left( \sum_{i=0}^{\infty} \rho(r) |\phi_i(z)|^2 e^{\beta(-i-\frac{1}{2})\hbar\omega_z} \right)^2}{\left[ \int dV \sum_{i=0}^{\infty} \rho(r) |\phi_i(z)|^2 e^{\beta(-i-\frac{1}{2})\hbar\omega_z} \right]^2} \quad (5)$$

in which  $\phi_i(z)$  is the  $i$ th eigenstate of the axial harmonic oscillator and  $\rho(r)$  is the classical thermal distribution in the radial direction, which is a Gaussian function. We confirmed that, for all the experimental conditions,  $V_{\text{eff}}^{(0)}$  differs from the more accurate  $V_{\text{eff}}^{(2)}$  by less than 20%. As it is unclear how this correction might interact with the larger correction from  $V_{\text{eff}}^{(1)}$ , we include  $V_{\text{eff}}^{(2)}$  only as an enlargement in the uncertainty.

### Hyperfine structure of NaLi

The Hamiltonian that includes hyperfine coupling and Zeeman energy is given as

$$H = H_{\text{HF}} + H_{\text{Zeeman}} \\ = a_1 \vec{S} \cdot \vec{I}_{\text{Na}} + a_2 \vec{S} \cdot \vec{I}_{\text{Li}} + \frac{\mu_{\text{B}}}{\hbar} (g_s \vec{S} + g_{I_{\text{Na}}} \vec{I}_{\text{Na}} + g_{I_{\text{Li}}} \vec{I}_{\text{Li}}) \cdot \vec{B} \quad (6)$$

in which  $a_1 = 433.2(1) \text{ MHz}$  and  $a_2 = 74.6(1) \text{ MHz}$  (ref. <sup>25</sup>). There are 36 states in the ground rotational state manifold ( $N = 0$ ). The states

# Article

converge to eight hyperfine thresholds in the zero-field limit owing to the conservation of the total angular momentum  $F = |\vec{F}| = |\vec{S} + \vec{I}_{\text{Na}} + \vec{I}_{\text{Li}}|$ , in which  $S = |\vec{S}| = 1$  is the total electron spin of NaLi( $a^3\Sigma^+$ ) and  $I_{\text{Na}} = 3/2$  and  $I_{\text{Li}} = 1$  are the nuclear spins of Na and Li, respectively. The hyperfine splitting owing to the Na nucleus is much larger than that owing to the Li nucleus, so  $F = |\vec{S} + \vec{I}_{\text{Na}}| = 1/2, 3/2$ , and  $5/2$  is an approximately good quantum number that characterizes the largest-scale hyperfine splittings in the zero-field limit in Extended Data Fig. 2. The hyperfine structure of NaLi in an external magnetic field is obtained by diagonalizing the Hamiltonian given in equation (6). A total of nine hyperfine states cross the lower stretched state at bias fields between 320 G and 340 G. There are three states that cross at fields within a few hundred mG of the resonance. Owing to the uncertainty of the hyperfine constants, the uncertainty of their energies relative to the stretched state is  $\pm 400$  kHz and therefore each of them is a possible candidate to cross the stretched state at or near the observed Feshbach resonance at 334.92 G.

The state  $a$  in Extended Data Fig. 3 is the lower stretched state ( $|F = 7/2, M_F = -7/2\rangle$ ), which has the spin character  $|M_s, M_{I_{\text{Na}}}, M_{I_{\text{Li}}}\rangle = |1, -3/2, -1\rangle$ . The three states close in energy near the resonance are indicated as  $b_1, b_2$  and  $b_3$  in Extended Data Fig. 3. The most probable candidate to couple to the stretched state is the state  $b_1 = |F = 5/2, M_F = -3/2\rangle$ , as its nuclear spin character overlaps with the stretched state by 50%, whereas for the other two states, in leading order, the spin overlap is zero. Non-zero nuclear spin overlap less than 0.1% may arise from small intramolecular spin–spin and spin–rotation couplings. More explicitly, the state  $b_1$  has spin contributions of 0.503 of  $|1, -3/2, -1\rangle$ , 0.324 of  $|0, -1/2, -1\rangle$ , 0.163 of  $|1, 1/2, -1\rangle$  etc. State  $b_2 = |F = 5/2, M_F = -1/2\rangle$  has 0.583 of  $|0, 1/2, -1\rangle$ , 0.301 of  $|1, -1/2, -1\rangle$ , 0.097 of  $|1, 3/2, -1\rangle$  and some other minor contributions. State  $b_3 = |F = 5/2, M_F = 1/2\rangle$  has 0.837 of  $|0, 3/2, -1\rangle$ , 0.145 of  $|1, 1/2, 0\rangle$  and some other minor contributions. The difference in  $M_F$  to the lower stretched state is the smallest for state  $b_1$ , which is 2.

## Long-range interactions of NaLi( $a^3\Sigma^+$ ) molecules

Here we show that the long-range coupling between the two hyperfine states  $|a\rangle$  and  $|b_1\rangle$  involved in the crossing shown in Extended Data Fig. 3 is too weak to explain the observed loss rates. To explain the observed Feshbach resonance, it is therefore necessary to assume the presence of a short-range loss mechanism. A minimal model for such a mechanism involves a bound state (channel  $|3\rangle$ ) coupled to the open channels ( $|aa\rangle$  and  $|ab_1\rangle$ ).

Long-range coupling would occur outside the centrifugal  $p$ -wave barrier of the input channel. The peak of the barrier is at  $24^{1/4} R_{\text{vdw}} \approx 7.8$  nm, at which the vdW length  $R_{\text{vdw}} = \frac{1}{2} \left( \frac{2\mu C_6}{h^2} \right)^{1/4}$  and the inner turning point is at 100 nm at a temperature of 3.35  $\mu\text{K}$ . In the Born approximation, for a potential of average strength  $V_0$  in an effective volume  $4\pi R_0^3/3$ , the total low-energy elastic-scattering cross-section  $\sigma = 4\pi \left( \frac{2\mu V_0 R_0^3}{3h^2} \right)^2$  (identical to the solution for a spherical square well potential with radius  $R_0$ ). Applying this relation to the observed nearly unitarity limited cross-section of  $2.95 \times 10^{-11} \text{ cm}^2$  corresponding to the loss-rate constant of  $10^{-10} \text{ cm}^3 \text{ s}^{-1}$  at 1  $\mu\text{K}$  and using the position of the inner turning point to estimate  $R_0 = 100$  nm provides a coupling matrix element  $V_0$  of 16 kHz. This is the required value for coupling outside the  $p$ -wave barrier to be compatible with the observed loss rates. For inelastic collisions with final wavevector  $k'$ , the rate has an extra factor  $k'/k$  owing to the density of states, but for large  $k'$ , the matrix element will decrease with  $k'$ , so our rough estimate for the required spatial coupling matrix element should also apply to inelastic collisions.

First, we show that magnetic dipolar interactions<sup>52</sup> that lead to spin exchange and dipolar relaxation and often limit the lifetime of magnetically trapped atoms are very weak outside the barrier. At the position of the  $p$ -wave barrier ( $R_b = 100$  nm), the interaction between two spins with magnetic moments  $2\mu_0$ , in which  $\mu_0$  is the Bohr magneton, is  $V_{\text{mDD}} = 0.052$  kHz, which is already small. However, owing to the selection

rules of the magnetic dipolar interaction ( $|\Delta M_s| = 1$ ), a single spin flip cannot provide coupling between the near-degenerate hyperfine states of interest  $|a\rangle$  and  $|b_1\rangle$ , which correspond to  $M_s = 1$  and  $M_s = -1$ , respectively (see above). Therefore the coupling must involve an intermediate state  $|k\rangle$ , which is off-resonant by its Zeeman energy  $\Delta_{ak} \approx 1\mu_0 \times 300 \text{ G} \approx 400$  MHz. This further reduces the magnetic dipolar coupling between the open channels by the factor  $(V_{\text{mDD}}/\Delta_{ak})^{-1} = 7.7 \times 10^6$  to much lower than 1 mHz. We can thus rule out the magnetic dipolar interaction as a source of the observed loss.

Spin flips in collisions of  $^3\Sigma$  molecules can also occur by means of coupling of the incident channels  $|a\rangle$  and  $|b_1\rangle$  to excited rotational states<sup>53,54</sup>. This mechanism is similar to that of magnetic dipolar relaxation discussed above, with the excited rotational states ( $N \geq 1$ ) playing the role of the intermediate Zeeman states. A distinctive feature of this mechanism is that it is mediated by the anisotropy of the electrostatic interaction between  $^3\Sigma$  molecules (which couples the  $N = 0$  incident states to  $N \geq 1$  closed-channel states of the same  $M_s$ ) and the spin–rotation and spin–spin interactions in the  $N \geq 1$  manifolds, which couple states of different  $M_s$ .

Below we quantify this molecular spin-relaxation mechanism by estimating the magnitude of the anisotropic coupling between the degenerate open channels  $|a\rangle$  and  $|b_1\rangle$  owing to the excited rotational states at  $R = 100$  nm. We find that the strongest coupling resulting from the electric dipole–dipole interaction is only 0.05 kHz and is therefore too small to explain the observed loss rate.

## Coupling matrix elements between degenerate open channels $|aa\rangle$ and $|ab_1\rangle$ owing to rotationally excited states

Here we estimate the matrix elements between the degenerate open channels  $|aa\rangle$  and  $|ab_1\rangle$  owing to long-range interactions between NaLi( $a^3\Sigma^+$ ) molecules. The interactions are described by the multipole expansion<sup>55</sup>

$$\hat{V}(\mathbf{R}, \mathbf{r}_A, \mathbf{r}_B) = (4\pi)^{3/2} \sum_{\lambda_A, \lambda_B, \lambda} V_{\lambda_A, \lambda_B, \lambda}(R, r_A, r_B) A_{\lambda_A, \lambda_B, \lambda}(\hat{R}, \hat{r}_A, \hat{r}_B) \quad (7)$$

in which  $A_{\lambda_A, \lambda_B, \lambda}(\hat{R}, \hat{r}_A, \hat{r}_B)$  are the angular functions,  $V_{\lambda_A, \lambda_B, \lambda}(R, r_A, r_B)$  are the radial expansion coefficients<sup>55</sup>,  $\hat{R} = \mathbf{R}/R$  and  $\hat{r}_i = \mathbf{r}_i/r_i$ . To leading order, the expansion (7) contains the electric dipole–dipole, dipole–quadrupole and quadrupole–quadrupole interactions. We assume that the internuclear distances of NaLi molecules are fixed at their equilibrium values. The rigid rotor approximation is expected to be extremely accurate because the long-range NaLi–NaLi interactions at  $R = R_b$  (see below) are thousands of times smaller than the spacing between the ground and the first excited vibrational states of NaLi ( $\hbar\omega_{10} = 40.2 \text{ cm}^{-1}$  (ref. <sup>56</sup>)). Because we are interested in long-range physics outside the  $p$ -wave barrier, we will also neglect the spin dependence of the NaLi–NaLi interaction, which is notable only at very close range ( $R \leq 10 a_0$ ).

The radial expansion coefficients in equation (7) are expressed in terms of the multipole moments  $Q_{\lambda_i, 0}$  of the interacting molecules ( $i = A, B$ )

$$V_{\lambda_A, \lambda_B, \lambda}(R, r_A, r_B) = \frac{Q_{\lambda_A, 0} Q_{\lambda_B, 0}}{R^{4+1}} \delta_{\lambda_A, \lambda_B} \frac{(-1)^{\lambda_A}}{[(2\lambda_A + 1)(2\lambda_B + 1)(2\lambda + 1)]^{1/2}} \left[ \frac{(2\lambda_A + 2\lambda_B + 1)!}{(2\lambda_A)! (2\lambda_B)!} \right]^{1/2} \quad (8)$$

The leading terms for two interacting neutral polar molecules such as NaLi are

$$\begin{aligned} V_{112}(R) &= -\frac{d^A d^B}{R^3} \sqrt{\frac{2}{3}} \text{ (dipole–dipole),} \\ V_{123}(R) &= -\frac{d^A Q_{20}^B}{R^4} \text{ (dipole–quadrupole),} \\ V_{224}(R) &= \frac{Q_{20}^A Q_{20}^B}{R^5} \sqrt{\frac{14}{5}} \text{ (quadrupole–quadrupole).} \end{aligned} \quad (9)$$

in which  $d^i$  and  $Q_{20}^i$  are the electric dipole and quadrupole moments of the  $i$ th molecule. Note that the long-range interaction (equation (7)) is spin-independent and hence can only couple the states of the same  $M_s$ ,  $M_{I_1}$  and  $M_{I_2}$ . We use the accurate ab initio value of the molecule-frame electric dipole moment  $d_{\text{NaLi}} = 0.167$  D (ref. <sup>56</sup>) and an approximate value of the electric quadrupole moment  $\Theta_{\text{NaLi}} = 10$  a.u. on the basis of the calculated values for  $\text{Na}_2$  and  $\text{Li}_2$  from ref. <sup>57</sup>. Our estimates are not sensitive to the precise magnitude of  $\Theta_{\text{NaLi}}$  because the dominant contribution at  $R = R_b$  is given by the electric dipole–dipole interaction.

Extended Data Fig. 4 shows the radial dependence of the long-range interactions between two NaLi molecules. Although the dipole–dipole interaction dominates outside the  $p$ -wave barrier ( $R \geq 100$  nm), both the dipole–quadrupole and quadrupole–quadrupole interactions grow in magnitude as  $R$  becomes shorter. At  $R = 100$  nm, the magnitude of the electric dipole–dipole, dipole–quadrupole, quadrupole–quadrupole and magnetic dipole–dipole interaction terms in equation (9) are (in kHz)  $V_{\text{DD}} = -3.446$ ,  $V_{\text{DQ}} = -0.339$ ,  $V_{\text{QQ}} = 0.0273$  and  $V_{\text{mDD}} = 0.0519$ , respectively.

Equating the barrier energy plotted in Extended Data Fig. 4 and the end points of the experimental range of collision energies (1.8–4.2  $\mu\text{K}$ ), we obtain the corresponding range of distances of closest approach of two NaLi molecules in the  $p$ -wave channel as  $R_b = 89.3$ –136.4 nm. For simplicity, we will use a value close to the middle of this interval,  $R_b = 100$  nm =  $1,890a_0$ , to estimate the magnitude of all long-range coupling matrix elements.

Having parameterized the anisotropic long-range interaction between two NaLi molecules (equation (9)), we now proceed to evaluate its matrix elements between the degenerate open channels  $|a\rangle$  and  $|b\rangle$ . The general matrix elements are given by:

$$\langle \gamma_A \gamma_B l m_l \eta | \hat{V}(\mathbf{R}, \mathbf{r}_A, \mathbf{r}_B) | \gamma'_A \gamma'_B l' m'_l \eta' \rangle \quad (10)$$

in which  $\langle \gamma_A \gamma_B l m_l \eta |$  are the properly symmetrized basis states for two identical molecules ( $\eta = -1$  for identical fermions),  $\gamma_A$  and  $\gamma_B$  refer to the internal hyperfine-Zeeman states of the molecules,  $l$  is the orbital angular momentum for the collision and  $m_l$  is its projection on the space-fixed quantization axis defined by the external magnetic field<sup>54</sup>. The initial scattering state of interest corresponds to  $\gamma_A = \gamma_B = a$ ,  $l = 1$ ,  $m_l = 0$  and  $\eta = -1$ .

The matrix elements are calculated by a straightforward extension of the procedure described in ref. <sup>54</sup> to include the hyperfine structure of both NaLi molecules (see the Supplemental Material of ref. <sup>58</sup> for more details about the basis functions). Using a minimal basis including three lowest rotational states of each of the NaLi molecules ( $N = 0$ –2) and two partial waves ( $l = 1, 3$ ) leads to the total number of coupled channels  $N_{\text{ch}} = 9,908$  for the total angular momentum projection  $M_{\text{tot}} = -7$ . We note that this basis set is expected to produce converged results at  $R = 100$  nm, at which the largest anisotropic long-range coupling  $|V_{\text{DD}}| = 3.446$  kHz is much smaller than the spacing between the  $N = 0$  and  $N = 1$  rotational levels ( $2B_e = 8.4$  GHz).

Extended Data Fig. 5 shows the matrix elements between the incident channel  $|aa, l=1, m_l=0\rangle$  at  $R = 100$  nm and all final channels. The largest of these matrix elements  $V_{01} \simeq 1.5$  kHz is due to the long-range electric dipole–dipole coupling between the ground and excited ( $N = 1$ ) rotational states. Although these matrix elements do not directly couple the degenerate channels  $|a\rangle$  and  $|b\rangle$ , they do contribute to indirect second-order couplings estimated below. There are also direct couplings between the incident channel and lower-lying relaxation channels (with single-molecule hyperfine-Zeeman states lower in energy than the incident state  $|aa\rangle$ ), which occur between the  $l = 1$  and  $l = 3$  partial waves. These couplings are mediated by the intramolecular spin–spin interaction, which couples the different  $M_s$  components of the  $N = 0$  and  $N = 2$  rotational states<sup>53</sup>. As shown in the inset of Extended Data Fig. 5, the largest of these direct couplings is about 0.04 kHz, which is too small to be responsible for the observed loss.

It remains to consider the second-order couplings between two degenerate channels  $|a\rangle$  and  $|b\rangle$  through rotationally excited states. These couplings are suppressed by the factor  $(V_{01}/\Delta_{01})^{-1}$ , in which  $\Delta_{01} = 2B_e$  is the energy of  $N = 1$  rotational states relative to the ground rotational state. Using the values  $\Delta_{01} = 8.4$  GHz and  $V_{01} = 1.5$  kHz, we obtain  $(V_{01}/\Delta_{01})^{-1} = 5.6 \times 10^6$  and thus the second-order couplings are smaller than 1 mHz and can be neglected.

### Fabry–Pérot transmission

The transmission of flux through a Fabry–Pérot cavity with two mirrors,  $M_1$  and  $M_2$ , is exactly expressed by an Airy distribution in terms of the incoming light intensity,  $I$ , mirror reflection and transmission coefficients,  $r_i$  and  $t_i$ , and single-pass phase shift  $\phi$ , as:

$$T_{\text{trans}} = I \frac{t_1^2 t_2^2}{(1 - r_1 r_2)^2 + 4 r_1 r_2 \sin^2 \phi}. \quad (11)$$

This Airy distribution is well approximated by a Lorentzian spectral line shape near a resonance ( $\omega - \omega_0$ ) for highly reflective cavities ( $r_1^2 r_2^2 \ll 1$ ) as:

$$T_{\text{trans}} = I \frac{\gamma_1 \gamma_2}{(\omega_0 - \omega)^2 + [(\gamma_1 + \gamma_2)/2]^2} \quad (12)$$

in which  $\gamma = -2 \ln r_i / \tau_{\text{RT}}$  are the mirror coupling strengths,  $\tau_{\text{RT}}$  is the round-trip time for a pulse travelling in the cavity,  $\omega_0$  is the angular frequency of the cavity mode and  $\omega$  is the angular frequency of the incoming light<sup>59</sup>.

Equation (12) also describes the dissipation in a harmonic oscillator driven by a friction force. A harmonic oscillator with resonance  $\omega_0$  and damping rate  $\gamma_2$  driven at frequency  $\omega$  through a frictional input coupling  $\gamma_1$  is described by the differential equation:

$$\frac{d^2 q(t)}{dt^2} + \gamma_2 \frac{dq(t)}{dt} + \gamma_1 \frac{d}{dt} [q(t) - q_d(t)] + \omega_0^2 q(t) = 0. \quad (13)$$

Here we assume the drive  $q_d(t) = q_0 \sin \omega t$ . By rearranging the terms, we obtain the standard equation of a driven harmonic oscillator with damping  $\gamma = \gamma_1 + \gamma_2$

$$\frac{d^2 q(t)}{dt^2} + \gamma \frac{dq(t)}{dt} + \omega_0^2 q(t) = \gamma_1 \frac{d}{dt} q_d(t). \quad (14)$$

The steady-state solution of equation (14) is

$$q(t) = \frac{\gamma_1 q_d \omega}{(\omega^2 - \omega_0^2)^2 + (\gamma \omega)^2} \cos(\omega t - \phi) \quad (15)$$

in which  $\phi$  is defined by  $\tan \phi = \gamma \omega / (\omega^2 - \omega_0^2)$ . The rate of energy dissipation owing to  $\gamma_2$  is  $P_{\text{out}} = \gamma_2 \dot{q}(t)^2$ . The average dissipation power

$$\langle P_{\text{out}} \rangle = \langle \gamma_2 \dot{q}^2 \rangle = \left\langle \gamma_2 \frac{\gamma_1^2 q_0^2 \omega^4}{(\omega^2 - \omega_0^2)^2 + (\gamma \omega)^2} \sin^2(\omega t - \phi) \right\rangle \quad (16)$$

is approximated to  $\frac{1}{8} \frac{\gamma_1^2 \gamma_2 q_0^2 \omega^2}{(\omega - \omega_0)^2 + (\gamma/2)^2}$  near resonance. The ratio of the average dissipated power normalized by a quarter of the average nominal drive power (drive power at zero amplitude of the harmonic oscillator) is exactly given by equation (12).

### Three-state $T$ -matrix model of $p$ -wave resonant scattering near degeneracies

The main purpose of this section is to provide a microscopic derivation for equation (2) using an extended nonperturbative  $T$ -matrix model of  $p$ -wave resonant scattering<sup>48</sup>. The model includes a single  $p$ -wave bound

# Article

state (or closed channel)  $|3\rangle$  coupled to two open channels: the incident channel  $|1\rangle$  and the outgoing inelastic channel  $|2\rangle$  with threshold energies  $E_1$  and  $E_2$  ( $E_1 > E_2$ ), as illustrated in Fig. 3a. The open channels are separated by the energy gap  $\Delta > 0$  such that  $E_1 = E_2 + \Delta$ . The total energy of the two-molecule system before the collision is  $E_1(k) = k^2/2\mu = k^2/m$ , in which  $\mu = m/2$  is the reduced mass of the two identical molecules of mass  $m$ ,  $k$  is the wavevector in the incident open channel  $|1\rangle$  and we have set  $E_1 = 0$ , so that  $E_2 = -\Delta$ . The incident scattering state in channel  $|1\rangle$  is a plane wave  $|\mathbf{k}\rangle$  with energy  $E_1(k) = k^2/m$  multiplied by the internal state vector of the colliding molecules  $|\alpha\rangle$ .

By summing the diagrammatic expansion for the  $T$  matrix, one obtains the following expression for the off-diagonal matrix elements between the open channels  $\alpha$  and  $\alpha'$  ( $\alpha, \alpha' = 1, 2$ )<sup>48</sup>

$$T_{\alpha, \alpha'} = \frac{C}{L^3} \frac{kk'F_\alpha(k)F_{\alpha'}(k')}{E - \delta - \Sigma_1 - \Sigma_2}, \quad (17)$$

in which  $E = k^2/m$  is the collision energy in the incident channel  $|1\rangle$  and  $\delta > 0$  is the energy of the bare  $p$ -wave bound state  $|3\rangle$ ,  $L^3$  is the quantization volume and  $C = \cos\theta$ , in which  $\theta$  is the angle between the incoming and outgoing wavevectors<sup>48</sup>. The functions  $F_\alpha(k)$  quantify the coupling between the open and closed channels as a function of the wavevector  $k$  and  $\Sigma_\alpha(E) = \frac{4\pi}{3}(2\pi)^{-3} \int q^4 dq \frac{|F_\alpha(q)|^2}{E - E_\alpha(q)}$  are the open–closed channel couplings in the energy space. These couplings are crucial, as they determine the resonance width. They can be evaluated by regularizing the diverging terms and then setting  $F(q) \rightarrow F(0)$ , which results in the following expression

$$\Sigma_\alpha(E) = \lambda_\alpha \frac{-i}{12\pi} m (m[E - E_\alpha(0)])^{3/2} - \delta_0^{(\alpha)} - \eta_\alpha [E - E_\alpha(0)] \quad (18)$$

in which  $\lambda_\alpha = |F_\alpha(0)|^2$  are the  $q \rightarrow 0$  limits of the open–closed channel couplings and the integrals

$$\delta_0^{(\alpha)} = (6\pi^2)^{-1} \int |F_\alpha(q)|^2 mq^2 dq \quad (19)$$

$$\eta_\alpha = (6\pi^2)^{-1} \int |F_\alpha(q)|^2 mdq \quad (20)$$

depend on the exact form of the coupling matrix elements between the open and closed channels. Note that (1)  $E_1(0) = 0$  and  $E_2(0) = -\Delta$  by definition and (2) the first term on the right-hand side of equation (18) is purely imaginary (because we assume  $\Delta > 0$ ) and thus gives rise to resonance width

$$\begin{aligned} \gamma(E, \Delta) &= (\gamma_1 + \gamma_2) + \gamma_d \\ &= -23m(\Sigma_1 + \Sigma_2) + \gamma_d \\ &= \frac{m^{5/2}}{6\pi} (\lambda_1 E^{3/2} + \lambda_2 (\Delta + E)^{3/2}) + \gamma_d \end{aligned} \quad (21)$$

in which we have introduced the intrinsic width  $\gamma_d$  of the  $p$ -wave bound state owing to the coupling to lower-lying inelastic channels other than  $|1\rangle$  and  $|2\rangle$  (see Extended Data Fig. 6a). Although ref. <sup>48</sup> assumes that  $\Delta$  is much larger than all the other energy scales in the problem, we do not make such an assumption here. Indeed, in our model, the new Feshbach resonance occurs when  $\Delta \rightarrow 0$ .

Defining the resonance shift  $\delta_0 = \delta_0^1 + \delta_0^2$  and neglecting the dimensionless terms  $\eta_\alpha$ , which are expected to be very small compared with unity<sup>48</sup>, we obtain from equation (17)

$$T_{\alpha, \alpha'} = \frac{C}{L^3} \frac{kk'F_\alpha(0)F_{\alpha'}(0)}{E - (\delta - \delta_0) + i\gamma(E, \Delta)/2}. \quad (22)$$

Here we have also assumed that the bound-continuum coupling matrix elements  $F(k)$  are well approximated by their zero- $k$  values  $F_\alpha(0)$ , which is a good approximation in the limit  $k \rightarrow 0$  (note, however, that this approximation starts to break down as  $kR_3$  approaches 1, in which  $R_3$  is the ‘size’ of the  $p$ -wave bound state, as shown below). The final wavevector in equation (22)  $k' = \sqrt{m(\Delta + E)}$ . We are interested in the two-body inelastic rate for the transition  $|1\rangle \rightarrow |2\rangle$  at fixed collision energy, which is given by (up to a constant scaling factor)

$$g_2(E, \Delta) = |T_{1,2}|^2 \rho_2(k') \simeq \frac{k^2 m (\Delta + E)^{3/2} \lambda_1 \lambda_2}{[E - (\delta - \delta_0)]^2 + \left[ \frac{m^{5/2}}{6\pi} \{ \lambda_1 E^{3/2} + \lambda_2 (\Delta + E)^{3/2} \} + \gamma_d \right]^2 / 4} \quad (23)$$

in which  $\rho_2(k') = (m/2)^{3/2} \sqrt{2(\Delta + E)}/2\pi^2$  is the density of states in the final channel  $|2\rangle$  (ref. <sup>60</sup>). Equation (2) is identical to equation (23) up to a constant overall scaling factor and with the intrinsic decay width of state  $|3\rangle$   $\gamma_d = 0$ . This provides a microscopic justification for the Fabry–Pérot model. In particular, the Fabry–Pérot decay rates may be expressed as  $\gamma_1 = \frac{m^{5/2}}{6\pi} \lambda_1 E^{3/2}$  and  $\gamma_2 = \frac{m^{5/2}}{6\pi} \lambda_2 (\Delta + E)^{3/2}$ , providing insight into their collision energy and  $\Delta$  dependence.

We now discuss the main features of the expression for the two-body inelastic rate equation (23). To this end, consider the expression for the resonance width  $\gamma(E, \Delta)$  in the denominator of equation (23) given by equation (21). As well as the intrinsic width  $\gamma_d$ , the width contains contributions from (1) the coupling between the incident open channel  $|1\rangle$  with the  $p$ -wave bound state  $\gamma_1 \propto E^{3/2} \propto k^3$  and (2) the coupling between open channels  $|1\rangle$  and  $|2\rangle$  through the bound state  $\gamma_2 \propto (E + \Delta)^{3/2} \propto (k')^3$ .

Equation (23) shows that the inelastic rate away from the resonance (when  $E - (\delta - \delta_0) > \gamma_1 + \gamma_2$  or for  $\gamma_d > \gamma_1 + \gamma_2$ ) exhibits the standard  $p$ -wave scaling  $g_2 \propto k_2(k')^3$  (ref. <sup>48</sup>), as observed experimentally. Normal  $p$ -wave threshold scaling will be modified if the denominator of equation (23) becomes energy-dependent, which requires the detuning  $E - (\delta - \delta_0)$  and  $\gamma_d$  to be small compared with  $\gamma_1 + \gamma_2$ . Under these (rather unlikely) conditions, the scaling changes to  $g_2(E) \propto k^2(k')^3 / [\lambda_1 k^3 + \lambda_2(k')^3]$ .

To further explore the properties of the inelastic rate in equation (23), it is convenient to introduce the parameter  $\tilde{\Delta} = \Delta + E$ , such that the translational energy in the outgoing channel  $|2\rangle$  vanishes at  $\tilde{\Delta} = 0$  ( $k' = 0$ ) and inelastic scattering becomes energetically forbidden at  $\tilde{\Delta} < 0$ . With this definition, we obtain from equation (23) the inelastic rate as a function of  $\tilde{\Delta}$

$$g_2(\tilde{\Delta}) \simeq \frac{(\tilde{\Delta})^{3/2}}{\delta E^2 + [\gamma_1 + c\tilde{\Delta}^{3/2}]^2 / 4}, \quad (24)$$

in which  $\delta E = E - (\delta - \delta_0)$  is the detuning from resonance,  $c = \frac{m^{5/2}}{6\pi} \lambda_2$  and we have omitted the factors proportional to  $k, m$  and  $\lambda_i$  in the numerator because we are interested in the inelastic rate at a fixed collision energy.

Note that our ability to vary  $\delta E$  by tuning an external magnetic field may be limited, as the magnetic moments of the closed-channel and open-channel  $p$ -wave states may be very close (as in the case of a single-channel  $p$ -wave shape resonance). We therefore do not assume the resonance condition and keep the term  $\delta E^2$  in equation (24).

Extended Data Fig. 6b shows that the inelastic rate  $g_2(\tilde{\Delta})$  has a pronounced resonance structure as a function of  $\tilde{\Delta}$ . The remarkable increase of the inelastic rate with narrowing the energy gap between the open channels is a consequence of the reduction of the total resonance width (equation (21)) in the limit  $\Delta \rightarrow 0$  at which  $\gamma_2 \rightarrow 0$  (note that we also require that  $\gamma_d \ll \gamma_1$ ). This reduction enhances the peak rate of inelastic decay of the  $p$ -wave bound state into channel  $|2\rangle$  above the universal limit.

The resonance profiles shown in Extended Data Fig. 6b are the sharpest at zero energy detuning ( $\delta E = 0$ ), at which the denominator of

equation (24) is most sensitive to  $\tilde{\Delta}$ . As expected, the resonance becomes more and more suppressed as one moves away from resonance, owing to the growing background contribution from the  $\delta E^2$  term in equation (24). In principle, the background contribution can arise not only from a finite  $\delta E$  but also from other mechanisms, such as the intrinsic decay of the *p*-wave bound states to deeply bound channels (parameterized by  $\gamma_d$ ), which may contribute to the overall decay rate in equation (21).

In the experiment, the temperature and observed width of the Feshbach resonance are similar. Therefore the strong dependence observed on  $\Delta$  suggests that alternative decay mechanisms are slow compared with the dominant decay channels, that is,  $\gamma_d \lesssim \gamma_i$  ( $i = 1, 2$ ). In principle,  $\gamma_d$  can be estimated from the line shape of the loss-rate constant in Fig. 2 as in ref.<sup>5</sup>. However, the resonance asymmetry is not resolved because of the magnetic-field inhomogeneity, which is comparable with or greater than the resonance width.

### Derivation of $F_\alpha(k)$ matrix elements

The *p*-wave bound state in channel |3⟩ is described by the wavefunction  $\langle \mathbf{R} | \psi_3 \rangle = \psi_3(\mathbf{R})$  of the intermolecular separation vector  $\mathbf{R}$ . For a single *p*-wave bound state, the radial and angular variables separate to give  $\psi_3(\mathbf{R}) = g_1(R) Y_{lm_u}(\hat{R})$ , in which  $m_u$  is the projection of the angular momentum  $l=1$  of the bound state on a quantization axis  $\mathbf{u}$ . As in ref.<sup>48</sup>, we assume that the bound state is coupled to both of the open channels | $\mathbf{k}, \alpha$ ⟩ ( $\alpha = 1, 2$ ) by means of the coupling matrix elements ⟨ $\mathbf{k}, \alpha | \mathcal{V} | 3 \rangle$ , in which | $\mathbf{R} | \mathbf{k} \alpha \rangle = e^{ikz} | \alpha \rangle$  are the scattering states in the open channels  $\alpha$ . Expanding the incoming plane wave in spherical waves,  $e^{ikz} = \sum_l i^l \sqrt{4\pi(2l+1)} j_l(kR) Y_{l0}(\theta, \phi)$ , in which  $j_l(kR)$  is a spherical Bessel function, we observe that only the *p*-wave ( $l=1$ ) components of the incident and outgoing waves couple to the *p*-wave bound state owing to the orthogonality of the spherical harmonics (and the assumption of isotropic bound-continuum coupling).

For practical purposes, it is convenient to define the bound-continuum couplings in  $k$ -space<sup>48</sup>

$$F_\alpha(k) = i\sqrt{12} \langle \alpha | \hat{V} | 3 \rangle \frac{1}{k} \int_0^\infty g_1^*(R) j_1(kR) R^2 dR \quad (25)$$

in which  $\langle \alpha | \hat{V} | 3 \rangle$  is a spin matrix element. The advantage of the  $F_\alpha(k)$  matrix elements is that they have a well-defined  $k \rightarrow 0$  limit. Expanding  $j_1(kR) \simeq kR/3 + O((kR)^5)$ , we get

$$F_\alpha(0) = i\sqrt{12} \langle \alpha | \hat{V} | 3 \rangle \frac{1}{k} \int_0^\infty g_1^*(R) R^3 dR \quad (26)$$

The approximation  $F(k) \simeq F(0)$  is used in the previous section and in ref.<sup>48</sup> to simplify the expression for the  $T$ -matrix elements near threshold. This approximation is valid as long as  $kR_3 \leq 0.1$ , in which  $R_3$  is the characteristic size of the *p*-wave bound state ( $g_1(R) \simeq R^2 e^{-R/R_3}$ ). We find that  $F(k) \simeq F(0)$  is a good approximation for the incident collision channel ( $kR_3 \simeq 0.1$  for  $R_3 = 100a_0$  and  $E = 10$  kHz). This is no longer the case when the open–closed splitting becomes large compared with the collision energy ( $\Delta/E \gg 30$ ) or the *p*-wave bound state becomes extremely delocalized, in which case the exact  $k$ -dependent matrix element  $F(k)$  should be used.

### Lifetime of collisional complex

For previously observed Feshbach resonances, one may estimate a lower limit for the lifetime of the collision complex by converting the observed width of the resonance to a lifetime. For our case of a 25-mG width, we get 29  $\mu$ s, using a magnetic-field sensitivity of 1 Bohr magneton to convert from magnetic field width to energy width. However, according to our model, the observed width may not reflect the width of the long-lived state but would depend instead on the ratio of coupling strengths for the two open channels. A more reliable estimate uses the

classical round-trip time  $\tau_{\text{RT}}$  for a zero-energy particle in the combined centrifugal and vdW potential, which is equal to  $\tau_{\text{RT}} = \hbar/E_{\text{vdW}} \approx 5.6$  ns with the vdW energy  $E_{\text{vdW}} = \frac{\hbar^2}{2\mu R_{\text{vdW}}^2}$ . The photon lifetime in a cavity is the round-trip time multiplied by the resonant enhancement divided by 4. Using this analogy and the observed loss-enhancement factor of 230, we obtain an estimate for the lifetime of the complex of 320 ns. We regard this as a low estimate. Even at the peak of the *p*-wave resonance, owing to thermal broadening, the maximum loss enhancement is reduced by a factor  $\hbar\gamma_1/k_B T$ .  $\gamma_1$  is estimated by the classical round-trip frequency  $1/\tau_{\text{RT}}$  multiplied by the quantum transmission probability  $|t_1|^2 \approx 2\bar{a}\bar{a}^2 k^3$  (ref.<sup>61</sup>). For a collision energy of 4.2  $\mu$ K, this is approximately  $2\pi \times 9$  kHz. Here  $\bar{a} = 4\pi R_{\text{vdW}}/\Gamma\left(\frac{1}{4}\right)^2$ ,  $\bar{a} = \bar{a}\Gamma\left(\frac{1}{4}\right)$  and  $k$  is the collision wavevector. Therefore the reduction factor is approximately 0.1, which implies a ten times larger lifetime. Furthermore, if we assume that the loss enhancement is possibly not 230 but 2,300 for 10% of the incident flux (model with polarization beam splitter), then the lifetime would be another factor of ten higher and could be tens of microseconds. The observed enhancement of 230 provides an upper bound for the short-range absorption coefficient  $\gamma \leq 0.0043$ .

### Data availability

The data that support the findings of this study are available from the corresponding author on reasonable request.

### Code availability

The codes used to generate the results are available from the corresponding author on reasonable request.

50. Son, H., Park, J. J., Ketterle, W. & Jamison, A. O. Collisional cooling of ultracold molecules. *Nature* **580**, 197–200 (2020).
51. De Marco, L. et al. A degenerate Fermi gas of polar molecules. *Science* **363**, 853–856 (2019).
52. Mies, F. H., Williams, C. J., Julienne, P. S. & Krauss, M. Estimating bounds on collisional relaxation rates of spin-polarized  $^{87}\text{Rb}$  atoms at ultracold temperatures. *J. Res. Natl Inst. Stand. Technol.* **101**, 521 (1996).
53. Krems, R. & Dalgarno, A. Quantum-mechanical theory of atom-molecule and molecular collisions in a magnetic field: spin depolarization. *J. Chem. Phys.* **120**, 2296–2307 (2004).
54. Tscherbul, T., Suleimanov, Y. V., Aquilanti, V. & Krems, R. Magnetic field modification of ultracold molecule–molecule collisions. *New J. Phys.* **11**, 055021 (2009).
55. Stone, A. *The Theory of Intermolecular Forces* 2nd edn, Ch. 3 (Oxford Univ. Press, 2013).
56. Gronowski, M., Koza, A. M. & Tomza, M. Ab initio properties of the NaLi molecule in the  $a^3\Sigma^+$  electronic state. *Phys. Rev. A* **102**, 020801 (2020).
57. Harrison, J. F. & Lawson, D. B. Quadrupole moments of the alkali dimers,  $\text{Li}_2$ ,  $\text{Na}_2$ , and  $\text{K}_2$ . *Int. J. Quantum Chem.* **102**, 1087–1091 (2005).
58. Hermansmeier, R., Ktos, J., Kotchigova, S. & Tscherbul, T. V. Quantum spin state selectivity and magnetic tuning of ultracold chemical reactions of triplet alkali–metal dimers with alkali–metal atoms. *Phys. Rev. Lett.* **127**, 103402 (2021).
59. Ismail, N., Kores, C. C., Geskus, D. & Pollnau, M. Fabry–Pérot resonator: spectral line shapes, generic and related Airy distributions, linewidths, finesse, and performance at low or frequency-dependent reflectivity. *Opt. Express* **24**, 16366–16389 (2016).
60. Friedrich, H. *Theoretical Atomic Physics* 4th edn (Springer, 2017).
61. Bai, Y.-P., Li, J.-L., Wang, G.-R. & Cong, S.-L. Model for investigating quantum reflection and quantum coherence in ultracold molecular collisions. *Phys. Rev. A* **100**, 012705 (2019).

**Acknowledgements** We thank J. Bohn for valuable discussions. We acknowledge support from the National Science Foundation (NSF) through the Center for Ultracold Atoms and grant no. 1506369 and from the Air Force Office of Scientific Research (MURI, grant no. FA9550-21-1-0069). Some of the analysis was performed by W.K. at the Aspen Center for Physics, which is supported by NSF grant PHY-1607611. J.J.P. acknowledges further support from the Samsung Scholarship. T.V.T. gratefully acknowledges support from the NSF CAREER award no. 2045681.

**Author contributions** J.J.P. carried out the experimental work. All authors contributed to the development of models, data analysis and writing the manuscript.

**Competing interests** The authors declare no competing interests.

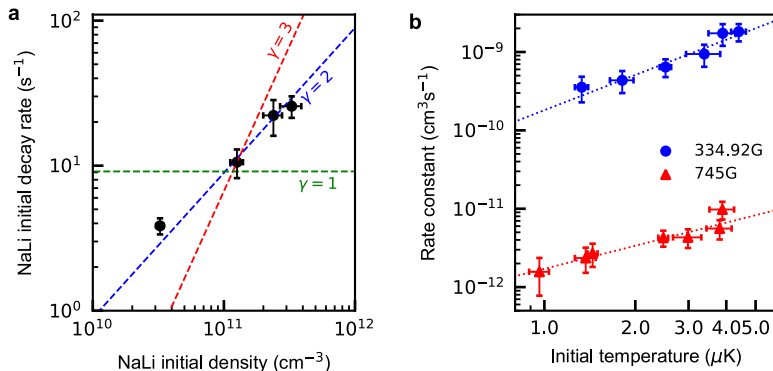
#### Additional information

**Supplementary information** The online version contains supplementary material available at <https://doi.org/10.1038/s41586-022-05635-8>.

**Correspondence and requests for materials** should be addressed to Julianne J. Park.

**Peer review information** *Nature* thanks the anonymous reviewers for their contribution to the peer review of this work. Peer reviewer reports are available.

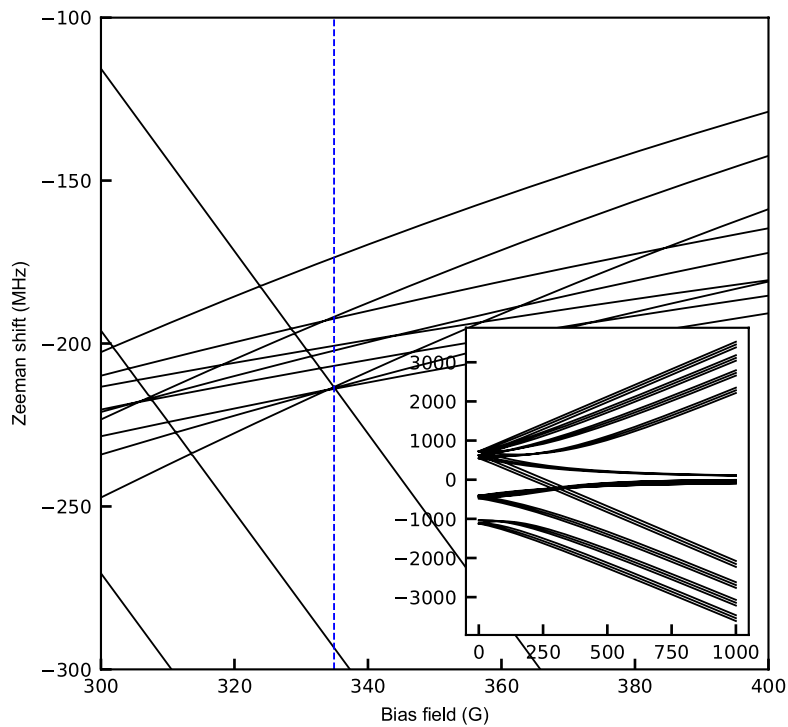
**Reprints and permissions information** is available at <http://www.nature.com/reprints>.



**Extended Data Fig. 1 | Density and temperature-dependent loss rate.**

**a**, Density dependency of molecular decay rate at 334.92 G. The initial decay rates are plotted as a function of initial molecule mean density. The green, blue and red dashed lines show the behaviour expected for single-molecule decay, two-body and three-body collisions, respectively. **b**, Threshold laws of molecule–molecule collisions. Initial rate coefficients are plotted as a function of the initial temperature of NaLi molecules. Blue data points are

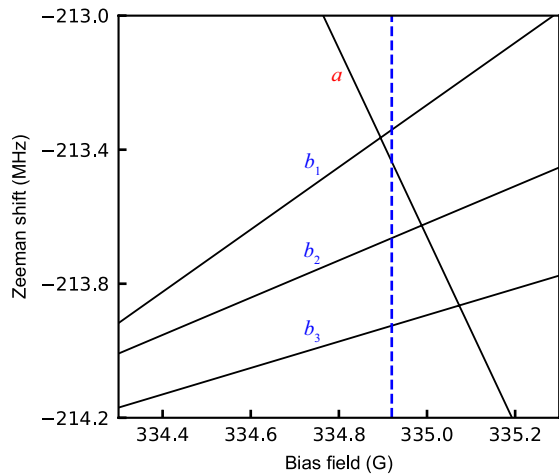
measurements near the centre of the resonance and red data points are measurements away from resonance near 745 G. The lines show the linear dependence expected for  $p$ -wave collisions. Data points were acquired from five to eight different hold times at each bias field; three to six measurements at a given hold time were averaged. Error bars represent one standard deviation of a fitted decay parameter.



**Extended Data Fig. 2 | Ground-state hyperfine structure in an external magnetic field.** The dashed vertical blue line indicates the position of the Feshbach resonance (about 334.92 G). The subplot shows the Zeeman energies

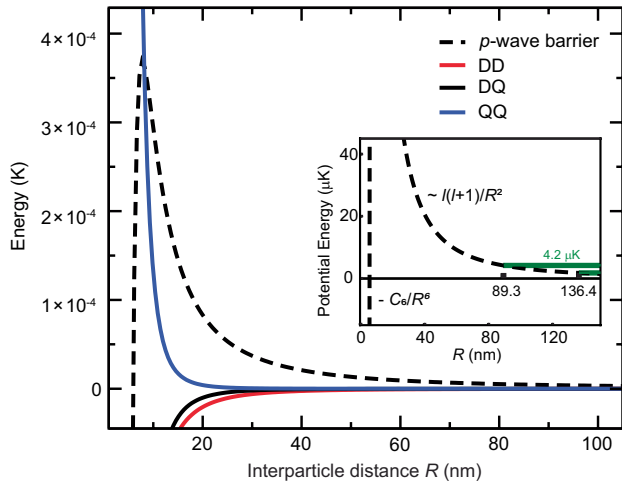
of NaLi hyperfine states from 0 to 1,000 G, whereas the main plot is zoomed into where there are nine near-degenerate hyperfine states (between 300 and 400 G).

## Article

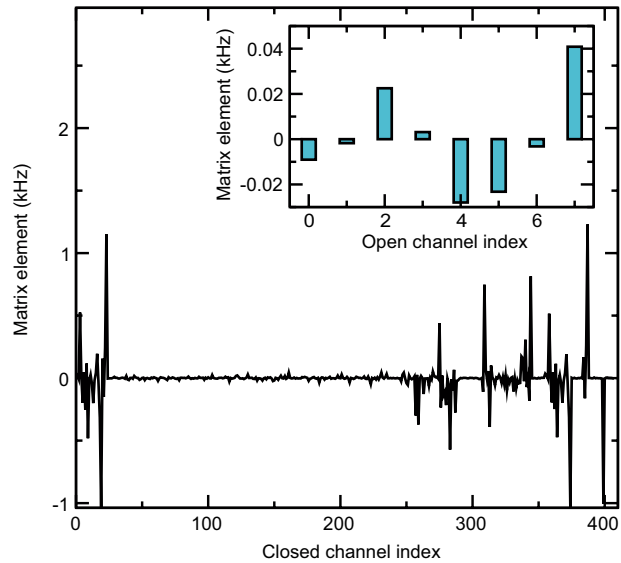


### Extended Data Fig. 3 | Ground-state hyperfine structure near 334.92 G.

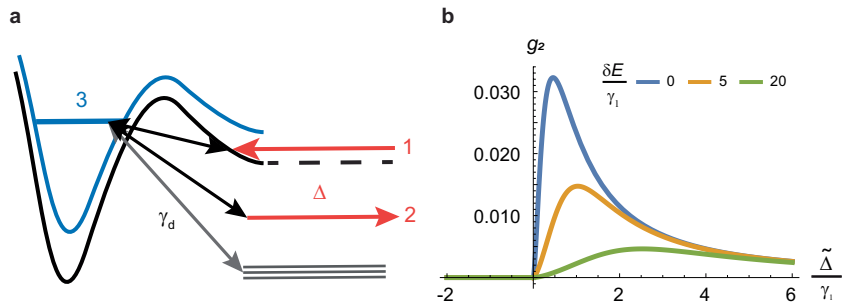
State  $a$  in red is the lower stretched hyperfine state of NaLi molecules. States  $b_1$ ,  $b_2$  and  $b_3$  in blue are other hyperfine states that are energetically close to state  $a$  near 334.92 G.



**Extended Data Fig. 4 | Radial dependence of NaLi–NaLi interactions.** Radial dependence of the dipole–dipole, dipole–quadrupole and quadrupole–quadrupole interactions of NaLi( $a^3\Sigma^+$ ) molecules. The  $p$ -wave centrifugal barrier is also shown (dashed line). The upper and lower bounds on the experimental collision energies (4.2  $\mu\text{K}$  and 1.8  $\mu\text{K}$ ) are marked by green horizontal lines. The turning points at the centrifugal barrier for these collision energies are  $R_b = 89.3$  and 136.4 nm, respectively.



**Extended Data Fig. 5 | Matrix elements of NaLi–NaLi interactions.** Matrix elements of the NaLi–NaLi interaction at  $R = 100$  nm as a function of the channel index labelling the basis states  $|\gamma_A\gamma_B, l m_l \eta\rangle$ . The initial channel is  $|aa, l=1, m_l=0\rangle$  and the total angular momentum projection  $M_{\text{tot}} = -7$ . The channel index labels closed channels, in which one or both NaLi molecules are in their  $N \geq 1$  excited rotational states. Only the matrix elements with the absolute magnitude exceeding 1 Hz are plotted. The magnetic field  $B = 333$  G is tuned near the crossing between the  $|a\rangle$  and  $|b_1\rangle$  hyperfine-Zeeman levels. Inset, histogram of direct coupling matrix elements between the incident channel and lower-lying open channels, in which both NaLi molecules are in the ground  $N = 0$  rotational states.



**Extended Data Fig. 6 | Degeneracy-induced resonance model.** **a**, Schematic of the resonance model with two open channels and a  $p$ -wave bound state trapped behind a centrifugal barrier. **b**, Inelastic rate  $g_2(\tilde{\Delta})$  (in arbitrary units)

plotted as a function of  $\tilde{\Delta}/\gamma_i$  for the different values of detuning from resonance normalized by  $\gamma_i$ ,  $\delta E/\gamma_i$ . Note that for  $\tilde{\Delta} < 0$ , the channel  $|2\rangle$  becomes closed and thus  $g_2(\tilde{\Delta}) = 0$ .